Science Advances

AAAS

advances.sciencemag.org/cgi/content/full/4/3/eaar4906/DC1

Supplementary Materials for

Near-field strong coupling of single quantum dots

Heiko Groß, Joachim M. Hamm, Tommaso Tufarelli, Ortwin Hess, Bert Hecht

Published 2 March 2018, *Sci. Adv.* **4**, eaar4906 (2018)
DOI: 10.1126/sciadv.aar4906

This PDF file includes:

Supplementary Text

Colloidal CdSeTe/ZnS quantum dots

CdSe have been used in studies that led to the first observations of blinking, power-law behavior and other non-linear effects in colloidal quantum dots (*18, 25, 49*). These properties and the simple synthesis process gave rise to CdSe nanocrystals being the basis for the majority of optical studies on colloidal quantum dots. The CdSe bulk bandgap of 1.8eV sets the upper limit of the exciton emission wavelength to 690nm. Decreasing the crystal size below the Bohr radius of 5.6nm increases the bandgap due to confinement (*50*). Changing the nanocrystal composition by doping is a common method to reduce the bandgap in order to reach the NIR regime. Tellurium has proven to be an ideal material in order to modify the intrinsic material properties (*51, 52*). Alloys of CdSe and CdTe (bandgap 1.55eV) can lead to a band gap smaller than that of the individual constituents (*53, 54*). Replacing even a single selenium atom with a tellurium atom already leads to measurable effects (*55*). The energy offset between the HOMO and LUMO levels of CdSe and CdTe yields a hole wave function which is more confined to the core while the electron remains delocalized. Increasing the Te concentration in CdSe in favor of Se continuously modifies the band gap until the QD consists of pure CdTe (*54*). A homogeneously alloyed quantum dot $CdSe_xTe_{1-x}$ exhibits a minimum bandgap of 1.35eV at a dopant ratio of x=0.34. In this work we use a specific type of quantum dots, i.e., commercially available CdSe quantum dots where tellurium is added to reach an exciton resonance wavelength beyond 690nm. For our nanocrystals CdSeTe/ZnS (QDot800 ITK Q21571MP, Thermo Fisher Scientific Inc., Waltham, USA) with a core diameter of about 6nm and an emission wavelength of 800nm quantum confinement still occurs due to an increased effective exciton Bohr radius. The ZnS shell serves mainly as chemical protection of the photoactive core, increases the photostability, and can also slightly redshift exciton wavelength (*56*).

The oscillator strength f of QDs is of importance for strong-coupling experiments as it contributes to the coupling constants via $g \propto \sqrt{f}$. It is expected that as the material composition is altered, the oscillator strength changes as well. The oscillator strength is usually determined either via fluorescence lifetime or absorption measurements. Here, however, we point out the importance of the fine structure of the band-edge exciton. The Coulomb interaction between the exciton electron and hole as well as crystal-structure anisotropy introduce a splitting of (in case of CdSe as well as CdTe) the eight-fold degenerate band edge transition (*28*). Emission of a photon is only possible for a dipole allowed transition (bright state). As these states are not necessarily the lowest in energy, thermal activation is required in order to populate the bright state (*57*). In the case of strong coupling with a broadband (plasmonic) resonator, all transitions can contribute to the coupling process (see fig. S19). We are therefore interested in the total oscillator strength of all transitions. The excited state lifetime τ can be used to deduce the oscillator strength corresponding to the single lowest optically active transition via

$$f = \frac{6m_e\varepsilon_0\pi c^3}{q^2 n\omega^2}\gamma_{rad}$$

where m_e is the electron mass, ε_0 is the vacuum permittivity, q is the electron charge, c is the speed of light in vacuum, n is the refractive index of the surrounding homogenous medium, ω is the transition frequency and γ_{rad} is the radiative decay rate ($\gamma_{rad} = 1/\tau$) (*58*). If the lifetime measurement is performed in a classical far-field emission/excitation scheme, the resulting oscillator strength solely refers to the lowest optically active transition while all other states do not contribute. Absorption measurements, on the other hand, are able to determine the oscillator strength of all available dipole allowed transitions. The challenge of these measurements is to isolate the light interaction of the QDs from parasitic contributions originating from unreacted precursors and organic ligands. This also complicates the determination of the exact molar concentration of the QDs.

The QDs which are used in the experiment exhibit an excited state lifetime of $(58 \pm 4)ns$. The measurements (data not shown) where performed on isolated QDs where we used time-tagged-time-resolved photon counting data to isolate the photons of the QD in the "ON" state from the ones in the "OFF" state. We thereby obtain a single-exponential decay, which allows us to determine the excited state lifetime with high precision. Standard methods rely on performing a multi-exponential fit which gives rise to a larger spread of reported values (*35, 58, 59*). Based on the measured lifetime, we assign a dipole moment $\mu = \sqrt{f\frac{\hbar}{2m_e\omega}}$ of about 5 Debye to the lowest optically active transition (*60*). In first approximation we assume that all eight transitions close to the band edge possess the same oscillator strength. The corresponding total oscillator strength is determined via $f_{eff} = \sum_k f_k$ as shown in fig. S19. This results in a total dipole moment of 15 Debye. Note that the exact order of the energy levels can depend on various properties such as QD shape and size and is therefore challenging to determine (*61–63*). However, precise knowledge about level spacing is not necessary as the broad plasmon resonance covers the complete band-edge fine structure.

It has been reported that during the synthesis the tellurium concentration in the center of the QD can be higher than in the rim region (*54*). Therefore the QD can be classified as a (quasi-) Type II QD (*64*). For the QD used in the present experiments such behavior may be present and is supported by two experimental observations. (i) For high excitation rates the QD exhibits a blueshift due to an increasing contribution of BX emission (see fig. S9). In Type I QDs (pure CdSe) typically the biexciton is considered as bound due to a positive interaction energy $\Delta_{XX} = 2E_X - E_{XX}$ (E_X and E_{XX} is the energy of the exciton and biexciton, respectively) and therefore redshifted with respect to the exciton resonance (*65*). The observed blueshift is related to a negative interaction energy due to the localized hole state caused by a higher Te density in the QD core (*32*). In addition, we (ii) measured a comparably long excited state lifetime (as mentioned above) (*58, 66*) which is an indication for a reduced electron hole overlap due to the confined hole wave function.

Fine structure splitting: The crystal structure of Te doped CdSe nanocrystals has been reported to be either wurtzite or zinc-blende which determines the energetic order of the fine structure states (*51, 52, 54, 67*). However, the QDs used in the present experiments possess a non-spherical shape which has been reported by TEM studies and was confirmed by our own SEM measurements (fig. S2C) (*47, 48*). This crystal anisotropy introduces changes to the fine structure that dominate over the crystal field splitting (*63*). Furthermore, due to reduced Coulomb interaction for larger QDs it is generally (not exclusively for a specific composition) observed that the fine structure splitting reduces as the QD radius increases (*65*). We therefore conclude that for our CdSeTe/ZnS QDs a total fine-structure splitting of $\Delta = 10 - 15meV$ is a reasonable assumption (*63*).
Charging/Trapping: The nanocrystal composition strongly affects optical properties such as exciton energy, Stokes shift and oscillator strength. However, the observation of fluorescence intermittency and the power law distribution of the "ON" and "OFF" times has been found to be independent of the QD material (*68*). It is therefore justified to equally apply fluorescence intermittency information gathered from measurements on one type of QD to different types of QDs.

FDTD Simulations

PNR resonance simulation

Using FDTD simulation, the spectrum of the PNR is determined by excitation at the antinode with a broadband electric dipole placed in the center of the gap. The far-field emission is detected in direction of the open end of the resonator. Temporal apodization of the detected emission suppresses contribution of the dipole excitation source. The first-order resonance (one node at the slit shortcut) lies in the IR spectral range. Figure S4A,B depict the mode profile of the second (one additional node) and third order (two additional nodes) resonance, respectively. The dependence of the resonance wavelength on the resonator length is shown in fig. S4C for a fixed gap width of 10nm. The second-order resonance emerges at a slit length of about 130nm with a resonance wavelength of 600nm and redshifts with increasing cavity length. At a length of 250nm, the third-order resonance appears following the same trend as the second-order mode. When increasing the gap width and keeping the length constant, the resonances are blueshifting and broadening (see fig. S4D). For our experiments we are aiming for small resonators at a wavelength of 800nm and we therefore use the second-order resonance. A simulated far-field spectrum is shown in fig. S4E. The simulation data (open circles) is fitted with a Lorentzian (red line) in order to accurately determine a linewidth and cavity decay rate of 51meV which corresponds to a Q-factor of 30. The narrow line width makes this kind of resonator ideal for strong coupling experiments at room temperature.

Calculating the coupling rate

The coupling energy $\mathcal{E}(r)$ between a (point) dipole μ at position **r** and the electric field is defined as

$$\mathcal{E}(\mathbf{r}) = \hbar \cdot g(\mathbf{r}) = \mu \cdot E_0(\mathbf{r})$$

where

$$E_0(\mathbf{r}) = \sqrt{\frac{\hbar\omega}{2\varepsilon_0 V_{eff}(\mathbf{r})}}$$

is the electric field per photon at the position of the dipole, $\hbar\omega$ is the photon energy, ε_0 the permittivity of free space, and $V_{eff}(r)$ the effective mode volume of the resonator mode. At the field maximum the effective mode volume equals the actual mode volume. For strong coupling, the absorption and emission process of the emitter locally modifies the field distribution of the resonant mode. As in our experiment the physical dimensions of emitter and resonator differ only by one order of magnitude, the field distribution and excitonic wavefunctions within the quantum dot should, in principle, be considered to obtain accurate values for the coupling energies. Unfortunately, such a description would require detailed knowledge of shape, material composition and electronic wavefunctions of the QDs. To obtain an estimate for the spontaneous emission enhancement, however, we treat it as a point dipole. Based on this assumption and the calculated modal field distribution we can then estimate the coupling constant for every position of the QD. Further details regarding the validity of this approach is discussed in the next section and fig. S6.

The physical volume of the PNR slit can be calculated: $10^{-22}\mathrm{m}^3$, which represents an upper limit of the effective mode volume since this corresponds to a mode with a homogenously distributed electric field throughout the resonator.

To obtain a more accurate result we determine the mode volume based on the field distribution in the resonator. The mode volume of plasmonic resonators is influenced by energy leakage via absorption in the metal and radiative emission. We follow the approach of Sauvan et al. to determine the effective mode volume of the quasinormal mode (QNM) in a resonator consisting of dispersive and dissipative materials (*69*) using

$$V_{eff}(r) = \frac{\int (\vec{E} \cdot \frac{\partial(\omega\varepsilon(r))}{\partial\omega}\vec{E} - \vec{H} \cdot \frac{\partial(\omega\mu(r))}{\partial\omega}\vec{H})dV}{2\varepsilon_0\varepsilon(r)\left|\vec{E}(r)\right|^2}$$

where $\varepsilon(r)$ and $\mu(r)$ are the relative permittivity and the relative permeability of the structure (resonator and environment), respectively. The fields $\vec{E}$ and $\vec{H}$ are the fields of the resonant QNM of the cavity, which we determine numerically using FDTD simulations by excitation with a Gaussian source. Values for the onset and width of the temporal window function were used according to Ge et al. (*70*) and perfectly matched layers (PML) boundary conditions were used to suppress backreflection of out-going radiative fields. An important aspect when simulating QNMs is the use of a homogeneous mesh. Introducing a refined mesh at the apex of the PNR reduces the local electric field amplitude which yields erroneous effective mode volumes. Convergence of the effective mode volume was obtained at a global mesh size of 0.6nm in accordance with a recent study (*10*) which showed similar results.

Our FDTD calculations include the QD as a dielectric sphere with a refractive index of 2.7 in order to account for the local field factor. This presence of a dielectric medium increases the local electric field and leads to a mode volume concentration (*40*). The effect is shown in fig. S5A where we plot the effective mode volume at the apex of the resonator with a logarithmic scale. Within the QD sphere the mode volume is reduced by almost two orders of magnitude. In fig. S5B we show a map of the corresponding coupling energy $\mathcal{E}(\mathbf{r})$ for a dipole moment of 15 Debye. The coupling strength can reach up to 100meV in accordance with our measurements. The coupling energy of the complete resonator is shown in fig. S5C (the dashed rectangle marks the region depicted in S5A,B). Figure S5D shows the coupling strength as a function of the mode volume and the dipole moment. These results indicate that for strong coupling with single transitions having dipole moments of 5 Debye extremely small mode volumes would be necessary. We therefore conclude that additional states at the band edge of the quantum dot are necessary in order to boost the coupling strength. Figure S19 shows the results of our detailed theoretical analysis on how several additional states near the band edge contribute to the coupling mechanism as one single effective level.

It is also important to note that the presented description of the mode volume is still an approximation as an unambiguous extraction of a single value is not possible. Furthermore, the calculation of QNMs does not account for the excitonic nature of the emitter. For single point-like emitters, such as dye molecules, the dipole approximation holds and the mode volume calculation at the location of the emitter allows to determine the coupling strength. An experimental confirmation was realized recently for the first time by Chikkaraddy et al. (*10*). For mesoscopic emitters, however, where the emitter's size becomes comparable to the spatial extension of the resonant field, the mode volume calculation becomes more complex.

To the best of our knowledge there are currently only two experimental studies about the coupling of localized plasmons of individual nano structures with single nanocrystals (*11, 71*). In the work of Hartsfield et al. the authors model the QD via a polarizable sphere with a largely overestimated dipole moment of 50 Debye in order to explain the changes to the scattering spectrum. Further information about the mode volume of the localized plasmon and how it is influenced by the quantum emitter has not been provided. Santhosh et al. presented a map of the calculated coupling strength at the gap region of a bowtie nano antenna reaching values of up to 200meV without any dielectric material to represent the QD. However, details about the mode volume or dipole moment have not been given and we were unable to reproduce their calculations. In fact, for a silver bowtie antenna with the same dimensions we calculate an effective mode volume on the order of $10^{-22}\mathrm{m}^3$ in the gap region which is about the same as for our cavity. So for a reasonable QD dipole moment the coupling strength is far below 200meV (see fig. S5D). The reason for this discrepancy might be due to differences in the field distribution between the results of the BEM calculations by Santhosh et al. and our FDTD calculations. In addition, their formalism to calculate the QNMs is based on the work of Koenderink (*72*) whereas we follow the approach of Sauvan et al.

Those recent advances in experimental realization of coupling single mesoscopic emitters with plasmonic resonances uncovers the challenge to unambiguously quantify the coupling rate. The implicit assumption that the plasmon mode distribution is maintained during strong coupling with a QD within the near field likely does not reflect the correct picture. In the next section we will show how the current formalism underestimates the coupling rate in case of a polarizable particle in close proximity to a near-field resonance.

Near-field proximity effect

The calculation of the mode volume is, as we discussed in the previous section, based on the unperturbed electric field distribution of the plasmonic resonator. However, in strong coupling of the mode with an excitonic material two hybridized modes emerge and further analysis based on the original uncoupled modes tend to be of limited validity (*4*). Here, we point out that it is to be expected that the original near-field distribution of the mode is modified due to near-field proximity coupling with the polarized QD.
To demonstrate this effect, the well-established strong coupling and associated mode hybridization of two interacting gold nanorods (length 120nm, diameter 30nm) is revisited in fig. S6A-F. To determine the coupling strength between two nanorods one may calculate the electric near-field distribution $E_{A,0}(\mathbf{r})$ for nanorod A (vacuum field). We assign a dipole moment μ_B to nanorod B based on its absorption cross-section on the order of $10^{-10} cm^2$ via the relation $\mu = \sqrt{\frac{3}{4\pi^2}\hbar\,\sigma_{abs}\,\gamma_0\,\epsilon_0\,\lambda}$ (*6, 73*). The resulting calculated coupling strength $g_{AB} = \mu_B \cdot E_{A,0}(\mathbf{r})$ only describes the observed mode splitting correctly as long as the rods are well separated and maintain a mutually unperturbed nearfield. Figure 6A shows the corresponding map of the coupling strength g_{AB} between nanorod A and a point dipole μ_B for various positions. A line cut across nanorod A is shown in fig. S6B (dark blue line).

With increasing distance x the coupling strength decreases proportional to the electric field. The horizontal line (light blue) marks the spectral width of the far-field spectrum of the rod $\kappa_{rod} = 64meV$. The condition for strong coupling is $g_{AB} = \Omega/2 > \kappa_{rod}$, where Ω denotes the Rabi splitting of the peaks in the strongly coupled system. We carried out FDTD simulations for discrete nanorod separations (center-center) to obtain the actual coupling strength $\Omega/2$ as a function of gap size (see fig. S6B, open circles) determined by fitting the resulting near-field spectra using two Gaussians.

For large separation (x=200nm) nanorod A is only slightly influenced by nanorod B resulting in a coupling strength $g_{AB} = 9meV$. The near-field distribution of the two rods is shown in fig. S6C and still roughly represents the superposition of two single-nanorod field distributions. Yet, the corresponding near-field spectrum (fig. S6D, blue line) already shows a deviation from the near-field spectrum of the isolated nanorod A (red line). The extracted splitting corresponds to a coupling strength of $25meV$, which is still in the weak-coupling regime.

In close proximity (nanorod separation 130nm) the near-field distribution is drastically changed and strongly deviates from just the sum of the fields of two isolated nanorods

(see fig. S6E). Due to near-field proximity coupling, the influential charge accumulation in the nanorod ends close to the gap, the near-field intensity in the gap is greatly enhanced. The original field distribution $E_{A,0}(\mathbf{r})$ is not maintained and therefore the definition of the coupling strength g_{AB} does not apply anymore. The calculated coupling strength of $28meV$ is much smaller than the actual coupling strength of the hybridized mode of $\Omega/2 = 124meV$ (see fig. S6F). Note that the actual mode overlap between the two rods is rather small as they approach each other end-to-end, which nonetheless can lead to an increased electric field inside the gap. As the coupling strength reaches the strong coupling condition in fig. S6B, the calculated coupling strength g_{AB} significantly underestimates the actual coupling strength because near-field proximity coupling is not taken into account.

This near-field proximity effect also affects the resulting coupling strength in the case of a plasmonic nanoresonator interacting with a mesoscopic quantum dot. In case of our plasmonic nanoresonator used in the experiment and a resonant quantum dot the situation is equivalent as the QD cannot be approximated as a point-dipole. In the far-field the coupling is described via the dipole moment of the quantum dot and the electric field distribution of the nanoresonator. However, when the mesoscopic QD approaches the near-field gradient of the nanorod the hybridization into two modes has an impact on the initial field distribution. In fact, the position outside the gap of the nanoresonator might be even more desirable to impact the initial field distribution.

Thus, the mutual interaction between the mode and the emitter sets a limit to the validity of the usual coupling strength calculation via the plasmonic mode volume. However, as the field in between the emitter and the plasmonic structure is likely to increase with proximity, the current approach is likely to underestimate the coupling strength. Therefore, we argue that the calculated coupling strength in the configuration of our experiment as depicted in fig. S5B matching the measurement only in the upper half of the QD sphere is a result of disregarding the QD polarizability.

Purcell Factor

The spontaneous emission rate of a dipole emitter in the near field of a plasmonic resonator is influenced by the local density of optical states (LDOS). The Purcell factor is the ratio of the emitter's emission rate with and without the resonator. A common approach to determine the Purcell factor via FDTD calculations is to monitor the emitted power of an electric point dipole. The fact that one simulation is necessary for each position of the dipole is a major drawback of this method. In order to obtain the LDOS distribution with one single simulation we use the approach proposed by Sauvan et al. (*69*). Figure S7 shows the spatial distribution of the Purcell factor where values as high as 10000 are readily achieved at the tip apex.

Excitation enhancement

The large Stokes shift provided by the QDs requires separate investigation of the PNR near field at the excitation and emission wavelengths. The spectral separation of almost 300nm can lead to significant differences in the field distribution especially since the excitation and emission are off- and on-resonant, respectively. In fig. S8A we show the resonant mode profile $E_{res}/E_{res,0}$ of a PNR in close vicinity to the PMMA layer excited with a Gaussian source (+z direction, x polarization) at a wavelength of 800nm. The field is apodized to remove any remaining contribution from the excitation source. Note that the value of the field strength is proportional but not equal to the coupling strength since the mode is not normalized. We observe that the field strength in the substrate increases towards the PNR probe. Whereas the coupling is proportional to the resonant field strength (E_{res}), the excitation rate is proportional to the excitation field intensity (${E_{ex}}^2$). In fig. S8B we show the excitation intensity profile $(E_{ex}/E_{ex,0})^2$ of the same structure after excitation in the same manner at 532nm without apodization. Note that now the highest excitation field in the substrate occurs close to the tip but decreases towards the slit of the cavity. The cross-sections at a depth averaged between 2 and 3nm below the surface is shown in fig. S8C. It is interesting to see that the excitation intensity $(E_{ex}/E_{ex,0})^2$ (pink line) has already dropped significantly at the position where the resonant field strength is highest (blue line). In the experiment this leads to the observation that the spectrum can still show features of strong coupling while the fluorescence intensity has already declined due to reduced excitation intensity.

Measurements

Absorption efficiency

The absorption efficiency of quantum dots (created excitons per incident photon) can be estimated via the size of the diffraction limited focus diameter and the absorption cross section of the quantum dots. At a wavelength of 532nm using a microscope objective with a numerical aperture of 1.45 we calculated a focus diameter of about 224nm. The absorption cross-section, extracted from saturation measurements of single quantum dots, is found to be $4 \times 10^{-15}\text{cm}^2$ in accordance with a recent study (*74*). The absorption efficiency for isolated quantum dots is therefore on the order of 10^{-5}. However, in proximity to a sharp gold edge, the local field enhancement leads to an increase of the effective absorption by about one order of magnitude to around 10^{-4}.

Measurements of isolated QD

We investigate the behavior of isolated QDs in a PMMA matrix on a glass substrate. When increasing the excitation rate above the saturation rate we observe a shift of the QD resonance due to increased biexciton (BX) generation (*75*). The BX resonance is slightly blueshifted with respect to the single exciton energy and dominates the emission processes for higher excitation rates. In fig. S9 we show the normalized spectrum of a QD being reversibly blueshifted by ramping the excitation rate up and down (spectra bottom to top). The magnitude of the resonance shift is comparable to the reported few tens of meV (*75*).

Influence of unstructured gold tip

Even without a PNR the presence of the gold tip in close vicinity to the QD affects its absorption and emission characteristics. Here, we experimentally studied the change of fluorescence and degree of polarization as well as spectral modifications of QDs in close proximity to an unstructured gold tip. Figure S10A shows an SEM image of the unstructured corner of a gold flake. The presence of the gold tip enhances the fluorescence as evident from the PL map in fig. S10B. We observe a fluorescence peak from an area smaller than the area associated with the diffraction-limit corresponding to the coupling of the tip with the QD. Next, we will show that the increased fluorescence rate can mainly be attributed to an enhanced excitation rate due to the enhanced electric near field at the apex of the tip.

By measuring both polarization components simultaneously we can calculate the degree of polarization (DOP) defined as $(E_{trans} - E_{long})/(E_{trans} + E_{long})$, where E_{trans} and E_{long} are the direction of the electric field components as indicated in fig. S10A. The DOP (fig. S10C) shows no significant change in presence of the gold tip. Note that emission enhancement due to coupling to a resonator would affect the polarization of the fluorescence depending on the character of the resonator mode (*76, 77*).

We analyze the spectral changes along the horizontal line in fig. S10B. The measured spectra (fig. S10D) are normalized and fitted with a Gaussian (dashed line). As the tip approaches the QD the fluorescence increases raising the signal-to-noise ratio. The amplitude and width of the peak are shown in fig. S10E where we observe a fluorescence enhancement of about 5. Furthermore, we notice a reduced peak width as the fluorescence reaches its maximum (spectrum #5). We attribute the reduced spectral width to the interaction of the tip and the QD in close proximity. It has been shown that a metallic tip can influence the charge distribution in a PMMA matrix giving rise to reduced spectral diffusion and narrower spectra (*31*). The spectral position of the resonance (see fig. S10F), however, remains unchanged in the presence of the tip. Emission into a resonant mode would alter the fluorescence spectrum as the spectrum is convoluted with the resonator. Since the spectra of different QDs with slightly different resonance remain unaltered we conclude that the bare tip has no resonance in the considered spectral window and that the enhanced fluorescence is mostly attributed to an increased excitation rate.

Note that the coupling to propagating surface plasmon modes does reduce the excited state lifetime. However, these modes propagate upwards along the gold flake and either decay non-radiatively due to ohmic losses or decay into photons which do not enter the microscope objective. Emission into these states is therefore not observed in our measurement and contributes to non-radiative quenching.

Weak-coupling regime

For the majority of PNRs the spectra of the coupled PNR-QD system only show a single peak, a behavior indicative for weak coupling. The enhanced fluorescence can be

attributed to (i) enhanced emission due to the resonant PNR as well as (ii) enhanced excitation as a result of the field enhancement caused by the metallic tip (similar to an unstructured gold tip, see fig. S10). The increased local density of optical states (LDOS) at the apex of the tip provides additional decay channels for the QD to radiate via the PNR mode into the far-field. In the weak-coupling regime spontaneous emission enhancement is described by the Purcell factor

$$F_P = \frac{3}{4\pi^2}\left(\frac{\lambda}{n}\right)^3 \frac{Q}{V}$$

where λ is the emission wavelength, n accounts for the surrounding refractive index, Q is the quality factor of the mode and V is the mode volume. FDTD simulations show that the Purcell factor at the open end of a PNR can reach a value of more than 10000 (see fig. S7). In fig. S11A, we show a large area PL map obtained with a weakly-coupling PNR centered in the laser focus. Narrow peaks superimpose the larger diffraction limited spots of the QDs. The corresponding DOP is shown in fig. S11B. We observe that the narrow peaks are mostly polarized in transverse direction (across the gap) indicating emission via the PNR. The polarization behavior produced by this kind of resonance has also been observed by Hancu et al. (*13*). In fig. S11C we demonstrate the achievable resolution as we show a smaller area which covers only one QD. A line cut through the center of the QD is shown in fig. S11D where we fitted the fluorescence profile with a Gaussian. The FWHM of the peak is less than 25nm. Note that this PL map was measured with high excitation rates in order to saturate the QD even during resonant coupling with the PNR. The peak width depends on the excitation rate and for resonant coupling is smallest for high pump rates. Further details on this aspect are shown in S13. Also note that using low excitation rates is usually preferential in experiments as it reduces blinking and yields cleaner PL maps. Furthermore, even though CdSeTe/ZnS QDs are known for their photostability, heavy incoherent excitation can eventually lead to bleaching or structural damage making further experiments on a pre-characterized QD impossible.

Figure S11E shows a PL spectrum of a PNR with a resonance wavelength of about 735nm. As in the strong-coupling case (Fig. 2D), for large QD-PNR separation the QD shows the unperturbed spectrum (fig. S11F, fitted with a Gaussian, dotted line). As the coupling increases (bottom to top), every frequency component of the QD is enhanced in agreement with the spectral line-shape of the resonator mode. The intensity increases as the QD-PNR distance decreases due to enhanced excitation and emission. Due to a blue-detuned PNR, the emission peak shifts accordingly until the spectrum strongly resembles the spectrum of the resonator mode (dashed line). The intensity eventually drops to small values (7th spectrum from bottom up) due to a spontaneous transition of the QD into a dark state.

Saturation threshold for excitation and emission enhancement

The fluorescence rate F for a two-level system can be described by

$$F = F_\infty \frac{I/I_S}{1 + I/I_S}$$

where I is the excitation rate, F_∞ is the fluorescence rate for infinitely large excitation rates and I_S is the saturation rate where the fluorescence rate equals $F_\infty/2$. Since F_∞ and I_S are proportional to the radiative decay rate γ, both, excitation and emission enhancement causes an increased fluorescence rate. However, the enhancement ΔF can be different depending on the relative magnitude between the excitation rate I and the saturation rate I_S.

Excitation enhancement solely alters the electric field at the position of the emitter and therefore increases the excitation rate. In fig. S12A we show the fluorescence characteristic of a single emitter. To observe a significant improvement of the fluorescence rate via excitation enhancement it is desirable to work below the saturation rate of the emitter in order to maximize the fluorescence boost (ΔF_{low}). The enhancement will be negligible above saturation since the limiting process is the spontaneous emission rate of the emitter (ΔF_{high}).

The opposite behavior is observed for emission enhancement which leads to a reduced lifetime of the excited state of the emitter and therefore increases the saturation rate. In fig. S12B we show the emission characteristic of an emitter with decay rates γ and 2γ indicated by the blue and red lines, respectively. Observation of a significant fluorescence rate change can only be expected for excitation rates in the regime far above the saturation rate of the isolated emitter (ΔF_{high}) where the fluorescence rate is limited by the saturation rate. Note that excitation above the saturation rate can turn into excitation below saturation for sufficiently enhanced decay rates. The emission rate below saturation is mainly limited by the excitation rate and any further reduction of the excited state lifetime has no significant influence on the fluorescence (ΔF_{low}).

In our experiment we move an emitter through the near field of a nanoresonator which causes a change in both, the excitation and emission rate. However, since the emission is resonant with the PNR, the modal emission enhancement becomes the main contributor to the increased fluorescence. The assumption of a fluorescence rate that is proportional to the LDOS of the mode (Purcell factor) is only valid for very large excitation rate. Since this is not the case in the experiment the fluorescence rate strongly depends on the excitation rate and the Purcell factor. In fig. S13 we show the fluorescence rate as a function of position based on different excitation rates and a Purcell factor following the shape of a Gaussian (dotted line). All graphs are normalized in order to demonstrate the change of fluorescence as function of position. Excitation rates of $I = \gamma_0$ are above saturation for an uncoupled emitter and therefore the emission is limited by the excited-state lifetime. However, as the coupling to the resonator increases the lifetime drops and the saturation rate increases dramatically rendering the fluorescence intensity limited by the excitation rate (dark blue solid line) before the maximum Purcell factor can be reached. As a consequence, the width of the fluorescence peak appears much broader than the pure Purcell factor profile. As the excitation rate increases (light solid lines), the

emission saturates at higher Purcell factors and causing a narrowing of the fluorescence profile.

In our measurement we observe a fluorescence profile broader than one would expect considering the actual mode field profile of the PNR. The low excitation rate between γ_0 and $10\gamma_0$ is likely to be the main reason for the broadening of the fluorescence profile. In addition, the large QD size and its high refractive index can lead to further broadening as it tends to concentrate field energy in close proximity to the PNR mode. Note that excitation enhancement due to the lightning rod effect causes a narrowing of the profile but is a comparably weaker effect.

PNR characterization for strong coupling

We simulate the plasmon resonances of the PNR slit based on its length and gap width. From SEM images we estimate a slit length of about 250nm and a gap width of 12nm (see fig. S14A). This specific PNR is slightly displaced with respect to the gold flake corner due to fabrication tolerances. This small asymmetry causes the right side of the resonator to be about 5nm longer than the left side.

We measured the spectrum of the PNR via the intrinsic photoluminescence (PL) of gold excited by a 532nm CW laser diode. A typical recorded emission spectrum of gold PL at the position of the PNR is displayed in fig. S14B (thin red line). We observe a significant background photoluminescence that stems from emission into modes associated with unstructured gold (dashed blue line). This contribution is modeled with an exponential decay since the spectral range is small compared to the broad tail of the overall PL of unstructured gold which peaks at about 500nm (*78*). On top of this background we observe a Lorentzian feature due to interaction with the PNR. Fitting a Lorentzian reveals that the resonance has a Q factor of 20 (black dash-dotted line). The sum of both contributions, indicated by the thick red line, provides good agreement with the measured data. The resonance frequency of the PNR obtained from the fit is found to be 1.59eV, slightly higher than the resonance energy used in the quantum-model (see main manuscript). We attribute this shift to the difference between near-field and far-field peak intensities (*79*). Similar observations have been reported when comparing gold PL spectra with white light scattering spectra which is attributed to the photoluminescence shaping mechanism (*80*). We note that the contribution of the resonant emission is rather small compared to the photoluminescence of unstructured gold. As the gap in the resonator gets smaller, the volume of gold penetrated by the resonant near field decreases (*15*) causing a reduced coupling with the mode and therefore less emission of gold PL via the PNR. In addition, the quadrupolar character of the mode causes a weak coupling to the far field leading to a further reduction of emission intensity. The measurement also confirms the assumption of a single resonator mode within the given spectral range.

Quantum-optical Model

Formulation of quantum-optical master equation

To reproduce the experimentally measured spectra both qualitatively and quantitatively we formulate a quantum-optical model for the coupled QD-PNR system based on the master-equation formalism (*81*). As discussed in the main manuscript, we interpret the four peaks observed in the strong-coupling spectra as a pair of Rabi doublets, arising from the coupling between the PNR and either neutral or charged states of the quantum dot. Therefore, the quantum dot should possess at least four internal (quantum) states that can coherently couple to the PNR. Furthermore, we must take into account the observed saturation of fluorescence versus pump power (see fig. S20). Such a nonlinear response cannot be attributed to the accumulation of multiple photons in the cavity since the pump rates used in the experiment are orders of magnitude below the loss rates of the system. Rather, it may be explained through the population of higher excited states of the quantum dot, which have no significant impact on the optical response of the system. Indeed, these optically inactive ("dark") states tend to decay non-radiatively due to the dominance of Auger recombination. In order to formulate a theory that is as simple as possible yet compatible with the above observations, we shall include a single dark state in our model. The QD is thus represented by a 5-level system with internal quantum states $|1\rangle, \dots, |5\rangle$ and associated bare energies $E_1, \dots, E_5$. We associate $|1\rangle$ with the neutral ground state, $|3\rangle$ with a single charged state, and $|5\rangle$ with a double charged dark state. States $|2\rangle$ and $|4\rangle$ are obtained by excitation of states $|1\rangle$ and $|3\rangle$ by one exciton, respectively, and are assumed optically active (see fig. S15). The dot is coherently coupled to a single EM field mode of the PNR (the cavity) with central frequency ω_0. As per standard procedure, excitations in the cavity are described via an annihilation operator a satisfying the bosonic commutation relation $[a, a^\dagger] = 1$. For convenience we formulate the Hamiltonian in the interaction picture, so that the center of the cavity resonance ω_0 is shifted to the origin of the frequency axis. The free (non-interacting) part of the Hamiltonian H_0, in units such that $\hbar = 1$, is thus chosen to be

$$H_0 = E_1|1\rangle\langle 1| + (E_1 + \omega_0)|2\rangle\langle 2| + E_3|3\rangle\langle 3| + (E_3 + \omega_0)|4\rangle\langle 4| + E_5|5\rangle\langle 5| + \omega_0 a^\dagger a$$

We next consider the coupling of the states via coherent and incoherent processes. As illustrated in fig. S15, the transition $|1\rangle \leftrightarrow |2\rangle$ ($|3\rangle \leftrightarrow |4\rangle$) is coherently coupled to the cavity field via the coupling rate $g_n(g_c)$. We introduced detuning factors between each transition and the cavity field, $\Delta_n = E_2 - E_1 - \omega_0$ ($\Delta_c = E_4 - E_3 - \omega_0$). Further transitions between the energy levels occur due to pumping and other incoherent processes, such as Auger recombination and spontaneous emission into other (non-cavity) modes. States $|3\rangle$, $|4\rangle$, $|5\rangle$ represent charged states of the quantum dot. Note that in absence of a cavity the transition $|3\rangle \leftrightarrow |4\rangle$ would be optically inactive due to its large non-radiative decay rate (attributed to Auger processes). In the coupled cavity-QD system this transition plays an important role as it becomes optically active due to an extremely strong coupling to the plasmonic cavity mode (at rate g_c), which is able to dominate over the non-radiative Auger processes (*82*). In contrast, the double charged state $|5\rangle$ is assumed to remain optically passive as Auger rates rapidly increase with the number of

charges/excitations in the QD (*83*). Crucially, occupation of this dark state at higher excitation powers yields saturation of fluorescence.

Taking into account all of the above, the density matrix of the composite system "quantum dot plus resonator" evolves under the following master equation in Lindblad form

$$\dot{\rho} = -i[H_I, \rho] + \frac{1}{2}\sum_k (2L_k \rho\, L_k^\dagger - L_k^\dagger L_k \rho - \rho L_k^\dagger L_k)$$

where the interaction picture Hamiltonian is given by

$$H_I = \Delta_n |2\rangle\langle 2| + \Delta_c |4\rangle\langle 4| + g_n(a|2\rangle\langle 1| + a^\dagger\, |1\rangle\langle 2|) + g_c(a|4\rangle\langle 3| + a^\dagger\, |3\rangle\langle 4|)$$

and describes the coherent processes taking place in our system. The "jump" operators L_k appearing in the master equation describe a variety of incoherent processes, which include pumping, incoherent energy transfer between the dot levels, as well as cavity loss, spontaneous emission, non-radiative Auger processes and dephasing. For convenience, we provide a list of the jump operators employed in our model, subdivided into categories.

Cavity leakage. characterized by a total decay rate κ including both radiative and non-radiative contributions

$$L_1 = \sqrt{\kappa} a$$

Dephasing. This is assumed to affect all internal states of the dot and is characterized by a rate γ_D (for simplicity assumed to be the same for all affected levels)

$$L_{11} = \sqrt{\gamma_D}|1\rangle\langle 1|$$
$$L_{12} = \sqrt{\gamma_D}|2\rangle\langle 2|$$
$$L_{13} = \sqrt{\gamma_D}|3\rangle\langle 3|$$
$$L_{14} = \sqrt{\gamma_D}|4\rangle\langle 4|$$
$$L_{15} = \sqrt{\gamma_D}|5\rangle\langle 5|$$

Pumping of the quantum dot at rate Λ

$$L_2 = \sqrt{(1-p_*)\Lambda}\,|2\rangle\langle 1|$$
$$L_3 = \sqrt{(1-p_{**})\Lambda}\,|4\rangle\langle 3|$$

where p_* (p_{**}) is the probability that the pump contributes to charging (double charging) of the quantum dot, i.e. the probability that it drives the incoherent transition $|1\rangle \dashrightarrow |3\rangle$ ($|3\rangle \dashrightarrow |5\rangle$), as opposed to exciting of the optically active level $|2\rangle$ ($|4\rangle$).

Spontaneous emission decay of the optically active excited states of the quantum dot into non-cavity modes at a rate Γ

$$L_4 = \sqrt{\Gamma}|1\rangle\langle 2|$$
$$L_5 = \sqrt{\Gamma}|3\rangle\langle 4|$$

Non-radiative decay of level 4

$$L_{10} = \sqrt{\gamma_A}|3\rangle\langle 4|$$

Where γ_A is a non-radiative decay rate associated with Auger processes.

Incoherent energy transfer between charged and neutral states of the quantum dot

$$L_6 = \sqrt{p_*\Lambda + \Lambda_*}|3\rangle\langle 1|$$
$$L_7 = \sqrt{p_{**}\Lambda + \Lambda_{**}}|5\rangle\langle 3|$$
$$L_8 = \sqrt{\gamma_*}|1\rangle\langle 3|$$
$$L_9 = \sqrt{\gamma_{**}}|3\rangle\langle 5|$$

The mechanisms of the dynamic charging processes in CdSeTe/ZnS QDs are complex and the mean lifetime distribution of the various charged states have been found to exhibit a power law dependency (*49*). This universal behavior has been subject to many studies to explain different experimental observations (*84–87*). Here we are interested in the steady-state spectra of the coupled system under cw-excitation rather than in the time evolution following pulsed excitation. We use a combination of pump-dependent and -independent rates to account for different charging mechanisms. The parameters Λ_*, Λ_{**} and γ_*, γ_{**} are the spontaneous trapping and release rates which account for the incoherent energy transfer between charged and neutral states of the dot, persisting even in absence of external pumping. These rates account for charging processes induced by hot electrons, which is a spontaneous process and therefore independent of the excitation rate (*21–25*). We assume that external pumping can contribute to charging processes through the rates $p_*\Lambda$ and $p_{**}\Lambda$, which account for multi-exciton processes such as Auger ionization (*88–94*).

Calculating the emission spectrum

Since we are dealing with a time-local master equation in Lindblad form (no explicit time dependence) we can employ the well-known Wiener–Khintchine theorem to calculate the stationary emission spectrum of the coupled system. In the strong-coupling regime, we assume that the dominant emission channel is provided by far-field emission of the cavity. In other words, we assume that the electric field amplitude entering the spectrometer is proportional to the cavity annihilation operator a. This implies that, up to a normalization constant, the observed spectrum $S(\omega)$ is given by (*95*)

$$S(\omega) \propto 2\mathrm{Re}\left(\int_0^\infty \langle a^\dagger(\tau)a(0)\rangle\, e^{-i\omega\tau} d\tau\right)$$

Employing the Quantum Regression Theorem (*81*), in the stationary regime we can formally write down the two-time correlation function $C(\tau) = \langle a^\dagger(\tau)a(0)\rangle$ as

$$C(\tau) = \mathrm{Tr}[a^\dagger e^{\mathcal{L}\tau} a\rho_\infty]$$

where $\mathcal{L}$ is the Lindblad superoperator implicitly defined by the master equation as per $\dot{\rho} = \mathcal{L}\rho$, and ρ_∞ is the steady state density matrix that needs to fulfil the conditions $\mathcal{L}\rho_\infty = 0, \rho_\infty \geq 0, \mathrm{Tr}[\rho_\infty] = 1$. Crucially, this treatment relies on the assumption of the existence of a unique steady state. The following expression can be derived for the steady state fluorescence spectrum

$$S(\omega) = -2\mathrm{Re}\left(\mathrm{Tr}[a^\dagger(\mathcal{L} - i\omega\mathbb{I})^{-1} a\rho_\infty)]\right)$$

where $\mathbb{I}$ is the identity superoperator. Note that $\mathcal{L}$ has a zero eigenvalue, due to the trace-preserving property of the master equation. Hence, the expression $(\mathcal{L} - i\omega\mathbb{I})^{-1}$ should be interpreted as the *pseudoinverse* of the operator $\mathcal{L} - i\omega\mathbb{I}$ to avoid a delta-like singularity at $\omega = 0$. In actual numerical calculations, we represent the annihilation operator a as a 2x2 matrix, which amounts to allowing at most a single photon in the cavity. We have verified numerically (and it can be checked easily by a back-of the envelope calculation given our experimental parameters) that the inclusion of higher photon numbers would not bring about significant quantitative changes in our analysis. Our combined system quantum dot + cavity is thus represented in a 10-dimensional Hilbert space.

We calculate the system spectrum through the well-known technique of *vectorization*: we map density matrices and operators into vectors of length 100, while the superoperator $\mathcal{L}$ is converted into a 100x100 matrix. $(\mathcal{L} - i\omega\mathbb{I})^{-1}$ thus amounts to a standard matrix inversion, while trace operations are mapped as $\mathrm{Tr}[AB] = \mathrm{vec}(A^\intercal) \cdot \mathrm{vec}(B)$, where A, B are two generic operators and vec() indicates the vectorization operation.

Contribution of neutral and charged states to emission

The neutral and charged state of the QD can be distinguished by the transition dipole moment. In fig. S16 we show a spectrum obtained from our model with equal contribution from the neutral and the charged state. The coupling strength for the neutral state (blue line) is set to 1 and for the charged (orange line) to 0.5. Even though both contributions are equal (same amount of photon emission), the contribution of the neutral state (blue line) to the total spectrum (black line) seems to be smaller than the one of the charged state (orange line) due to the larger peak separation. In fact, the observed similar contribution is in accordance with experimental studies on isolated QDs reporting similar occurrence probabilities of the neutral and charged state (*96*, *97*).

Reversibility of detuning in strong coupling regime

In the experiment, increasing the excitation rate can be used to tune the emitter resonance as the emission of the QD gradually changes from exciton to biexciton emission (*75*). We confirmed this behavior by measuring uncoupled QDs and observe a gradual and reversible blueshift of the spectrum with increasing excitation rate. In the strong-coupling regime we are able to observe the same effect which results in a blueshift of the peaks with increasing power and a redshift with decreasing power (see fig. S17, gray lines, bottom to top). In our model we use the detuning parameter of the neutral and charged state to tune the QD resonance and are able to reproduce the measured spectra (red lines).

High-power spectrum comparison between different QDs

The spectrum of the strongly coupled system is significantly affected by the exciton resonance and the dipole moment of the QD. We measured the spectrum at high excitation rates of five different QDs which are quickly approached consecutively in order to avoid a probe drift. In fig. S18 we show the measured spectra (open circles) and the corresponding fit with the model (solid lines) ordered according to the detuning between exciton and cavity resonance. While the highly asymmetric spectra are explained by a strong detuning, we also observe different coupling strengths as apparent from the variation of peak splitting. Both observations can be explained by deviations in size and orientation of the chemically grown QDs. Furthermore, the fitting of the model showed minor differences in the cavity resonance which can be attributed to a slight deformation of the PNR geometry while sliding over the substrate during the fast sequential QD approaches.

Multi-Level-Emitter Quantum model

Here we show how, at our experimental conditions, a multiplet of closely spaced excited sublevels may be well approximated by a single effective energy level, featuring an enhanced coherent coupling to the cavity field. Note that such coupling-enhancement effect is analogous to what occurs in the well-known phenomenon of "Dicke superradiance", with the important difference that in the latter case one considers N identical emitters coherently coupled to the same field, as opposed to our case of N (approximately) degenerate levels of a single emitter (*98, 99*). A recent theoretical study explored the case of two detuned orthogonal dipole moments strongly coupled to a photonic crystal (*39*).

For the purposes of this section we shall only focus on modelling the $|1\rangle \leftrightarrow |2\rangle$ transition of the quantum dot and the associated coupling to the cavity. A straightforward, yet cumbersome, extension of the model below may be devised to include the $|3\rangle \leftrightarrow |4\rangle$ transition, but such generalization is here omitted for brevity.

As before, we label the electronic ground state of our emitter as $|1\rangle$, while state $|2\rangle$ is now replaced by a collection of N sublevels $|e_k\rangle$, where $k = 1, \dots, N$. For simplicity, each transition $|1\rangle \leftrightarrow |e_k\rangle$ is coupled to the cavity mode with the same strength g, the

extension to different coupling constants being straightforward. We emphasize that some of the considered transitions may be dipole-forbidden (e.g. some may be quadrupole-allowed), yet they could be activated by strong spatial gradients in the resonator's nearfield (see figure S5B). As before we assume that the cavity resonance has a central frequency ω_0, while the energy of the ground state $|1\rangle$ can be set to zero without loss of generality. Each sublevel $|e_k\rangle$ is characterized by a transition frequency $\omega_0 + \Delta_k$, where Δ_k is the detuning with respect to the cavity field. The coherent interaction between emitter and field is described by the following "microscopic" Hamiltonian (recall that $\hbar = 1$)

$$H_{mic} = \omega_0 a^\dagger a + \sum_{k=1}^{N} (\omega_0 + \Delta_k) |e_k\rangle\langle e_k| + \sum_{k=1}^{N} g(a|e_k\rangle\langle 1| + a^\dagger|1\rangle\langle e_k|)$$

We may immediately notice that, if the sublevels were exactly degenerate, that is $\Delta_k = \Delta$ for all k, one could define $|2\rangle = \frac{1}{\sqrt{N}} \sum_{k=1}^{N} |e_k\rangle$ as the only linear combination of sublevels that couples to the cavity field, with an effective, and enhanced, coupling constant $g_{eff} = \sqrt{N} g$. In such highly symmetric conditions, all other combinations of the sublevels would not contribute to the optical response of the system. One could hence simplify the quantum dot description by only retaining the internal levels $|1\rangle$ and $|2\rangle$, coupled to the cavity via an effective Jaynes-Cummings Hamiltonian

$$H_{eff} = \omega_0 a^\dagger a + (\omega_0 + \Delta)|2\rangle\langle 2| + g_{eff}(a|2\rangle\langle 1| + a^\dagger|1\rangle\langle 2|)$$

In our experiment, the sublevels $|e_k\rangle$ are not exactly degenerate and may feature different detunings Δ_k in the range of 10meV. Yet, our estimated detuning range is one order of magnitude smaller than the effective coupling constant g_{eff}, while the presence of dephasing processes tends to broaden the sublevels and increase their spectral overlap. Hence, we now show that the effective Hamiltonian H_{eff} still provides a sufficiently good approximation for our purposes.

In fig. S19A-H we compare the cavity emission spectra predicted by the two Hamiltonians H_{mic} and H_{eff} (for the latter we fix $\Delta = \sum_k \Delta_k / N$, i.e. the average detuning of the sublevels). For spectral calculations we again resort to the master equation techniques, including in both cases cavity decay at rate κ, as well as the dephasing of all excited sublevels at rate γ_D. We include a pump term of the form $\sqrt{\Lambda}\,|e_n\rangle\,\langle 1|$ ($\sqrt{\Lambda}\,|2\rangle\,\langle 1|$) for the H_{mic} (H_{eff}) case. The pumping populates the state $|e_n\rangle$, which is the highest state of the fine structure. This is in accordance with the experiment where we create high energy excitons which undergo relaxation until they reach the upper level of the fine structure. In the case of a single level with coupling strength $g = 36meV$ (fig. S19A), the cavity (orange line) and the exciton (black line) are on resonance ($\Delta_1 = 0meV$). The corresponding spectra calculated with the two Hamiltonians H_{mic} and H_{eff} (blue solid and red dashed line, respectively) yield exactly the same result ($\kappa = 78meV$, $\gamma_d = 57meV$). The system is on the verge to strong coupling as the Rabi splitting is already visible ($g_{eff} = g = 36meV$). Adding an additional level with the

same coupling strength g ($\Delta_2 = 1.25meV$) shows an increase in total coupling strength as indicated in fig. S19B. Since the highest level is blueshifted with respect to the cavity, the resulting spectrum calculated with H_{mic} exhibits an asymmetry. The spectrum with the Hamiltonian H_{eff} represents the case with a single transition is on resonance with an effective coupling strength of $g_{eff} = \sqrt{2}g$. Including up to eight levels (fig. S19H) shows an increasing separation of the two Rabi peaks while maintaining exceptional good agreement between the two models. Notice how the pumping of the highest fine structure level yields a small asymmetry in the spectrum associated with H_{mic}, but the difference between the spectra predicted by the two models is hard to appreciate. The comparison between the two models clearly shows how the fine structure of quantum dots can contribute to the coupling of broadband plasmon resonances by boosting the coupling strength via an effective oscillator strength $f_{eff} = \sum_k f_k$.

We also show in fig. S19I-P how the superposition of two independent multilevel systems evolves as the coupling strength is increased by adding additional levels. This case relates to the experiment where two QD states with different coupling strength are strongly coupled with the cavity. In fig. S19I we show the superposition (purple solid line) of two strongly coupled systems with a coupling strength of $g_1 = 36meV$ (gray dashed line) and $g_2 = 13meV$ (black dashed line) each containing a single excited state. Adding additional states (fig. S19J-K) increases the effective coupling strength and shows the transition into a four peaked spectrum with a slight amplitude asymmetry.

Saturation during strong coupling

We observe saturation of the emission for excitation rates in the GHz range, three orders of magnitude below the coupling rate. Figure S20 exhibits the saturation behavior of three different QDs coupled to the plasmonic nanoresonator as manifested in the dependence of the integrated spectra (marker) on the excitation rate (range 1MHz to 20GHz). At these high excitation rates, the probability for multi-exciton generation increases significantly. Due to the rapid increase of Auger rates with the number of excited charge carriers multi-exciton states eventually become dark – even in the strong coupling regime (*83*). It is this effective shelving into Auger-quenched dark states which is responsible for the observed saturation behavior. Indeed, upon inclusion of a non-radiative state, the quantum-optical model reproduces the saturation behavior in good agreement with the experimentally measured data.

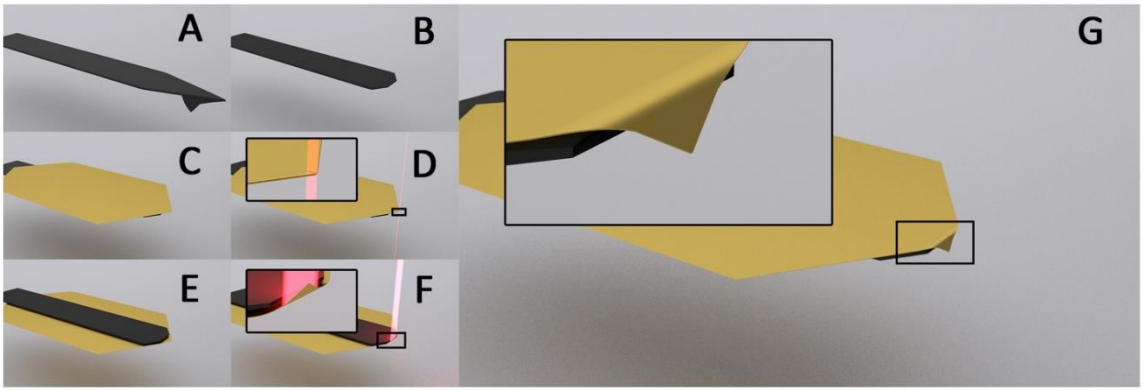

fig. S1. Scanning probe fabrication. (**A**) Commercial contact-mode cantilever without reflection coating. (**B**) Cantilever after cutting of the tip via focused-ion beam milling. (**C**) Deposition of a single-crystalline gold flake using a needle attached to a micromanipulator (not shown). (**D**) Fabrication of the PNR by a single FIB cut. (**E**) Back side of the probe. (**F**) Large-area ion beam irradiation induces strain in the flake and causes bending. (**G**) Final scanning probe with PNR as the foremost part.

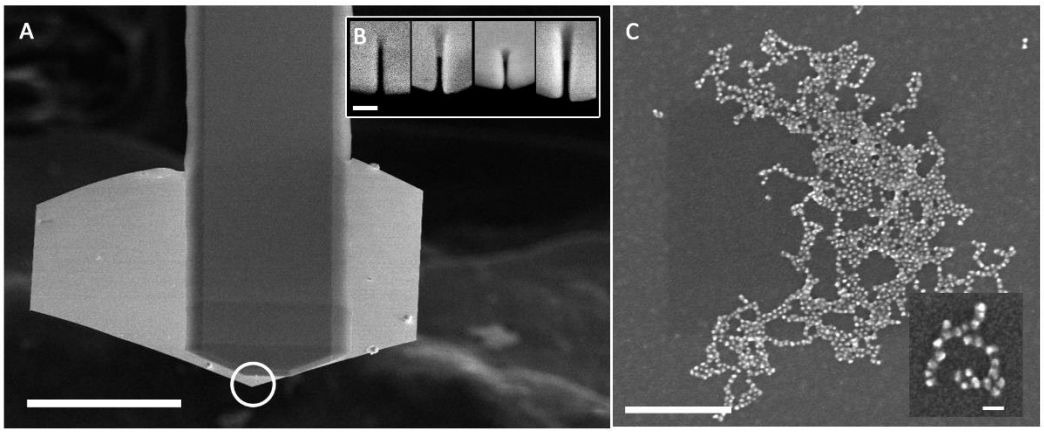

fig. S2. SEM characterization. (**A**) SEM image of the AFM contact mode cantilever after tip removal and flake deposition (scale bar 50µm). (**B**) SEM images of a variety of PNRs fabricated at the gold flake corner (white circle in A). Depending on the flake thickness the width of the resulting slit can vary (scale bar 100nm). (**C**) SEM image of the employed quantum dots (scale bar 250nm). The QD sample was prepared via drop casting on a copper substrate and does not reflect the distribution of quantum dots in the samples used for strong-coupling experiments. Inset: Zoom-in indicates the non-spherical shape (scale bar 25nm).

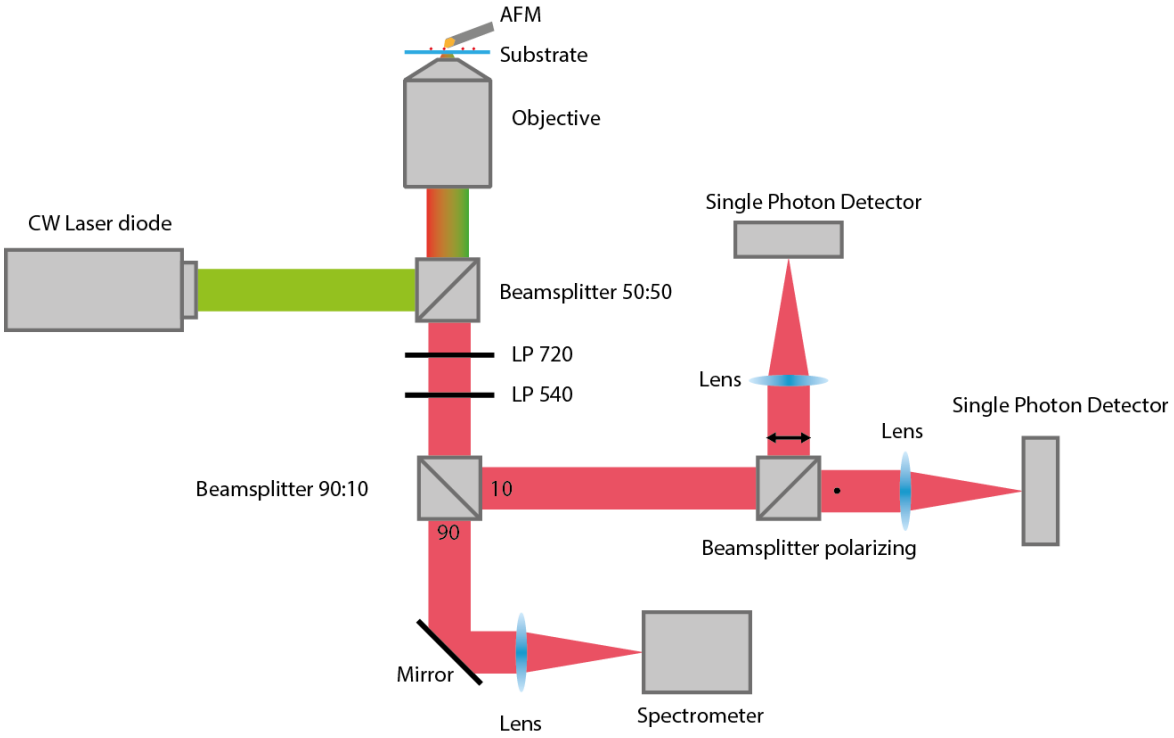

fig. S3. Schematic of the optical setup.

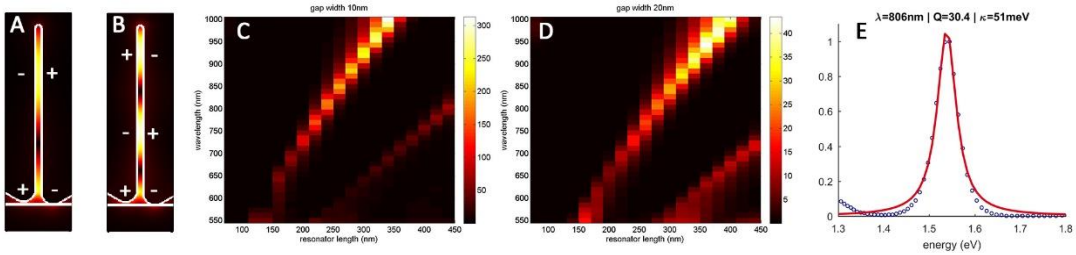

fig. S4. Simulated mode profiles and far-field spectra of PNRs for different gap widths and slit lengths between 80 and 440 nm. (**A**-**B**) Mode profile of the second- and third- order resonance, respectively. (**C**-**D**) Far-field spectra of the PNR with lengths between 80nm and 440nm and gap widths of 10nm and 20nm, respectively. (**E**) Simulated far-field spectrum of a PNR with a gap width of 10nm.

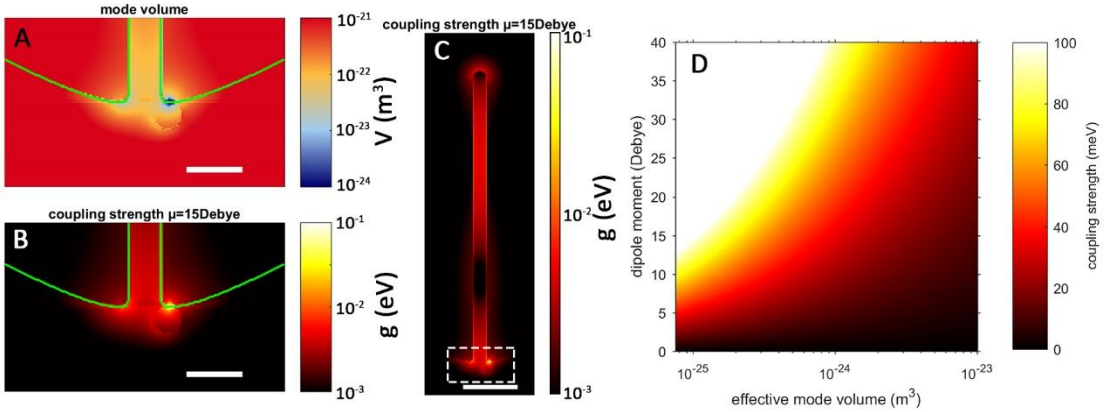

fig. S5. Calculating the coupling strength. (**A**) Effective mode volume at the apex of the tip. The mode volume is drastically concentrated within the quantum dot due to the increased refractive index. (**B**) Map of the coupling strength $g(r)$ with a QD modeled as a dielectric sphere near the PNR apex (scale bar: 20nm). (**C**) Overall coupling strength of the resonator (white dashed rectangle marks the region of interest in **B**. (Scale bar: 50nm.) (**D**) Coupling strength as a function of mode volume and dipole moment.

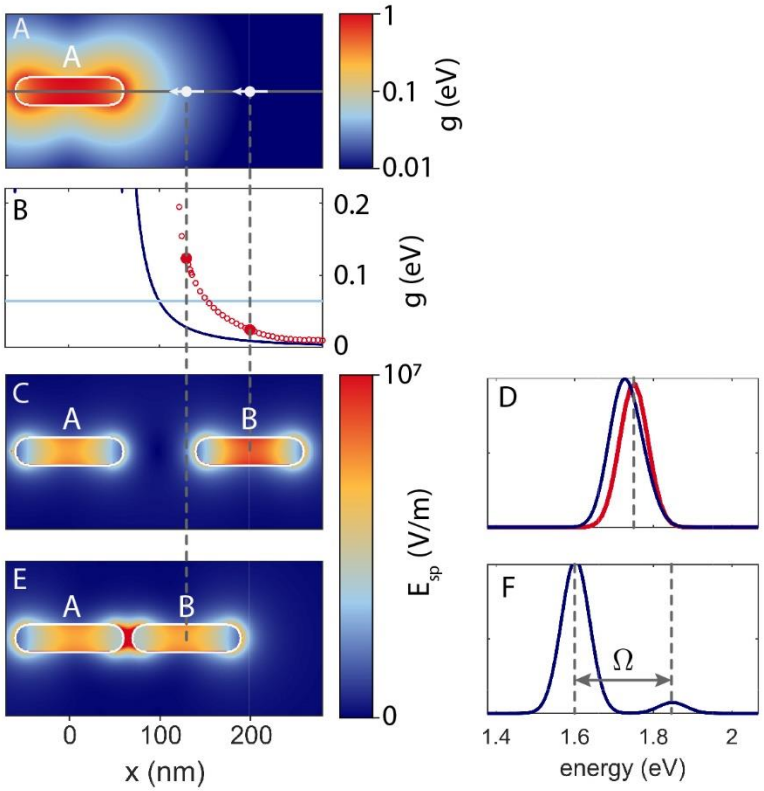

fig. S6. Near-field proximity coupling. (**A**) Coupling strength map between a single gold nanorod and a point dipole $\mu_B = 4000\ Debye$. (**B**) Line-cut of the coupling constant (dark blue line) in **a** along the longitudinal axis of nanorod A. The open circles indicate the coupling strength extracted from FDTD simulations. The horizontal light blue line shows the near-field spectral width κ_{rod} of a single nano rod. (**C**) Vacuum field distribution of two rods (gap size 80nm). (**D**) Near-field spectrum (at 1.6eV) of a single isolated gold nanorod (red) and two coupled gold nanorods with a gap size of 80nm (blue). (**E**) Electric field distribution of two hybridized nanorod modes (gap size 10nm). (**F**) Near-field spectrum of the mode shown in **E**. The resonance is shifted by 149meV.

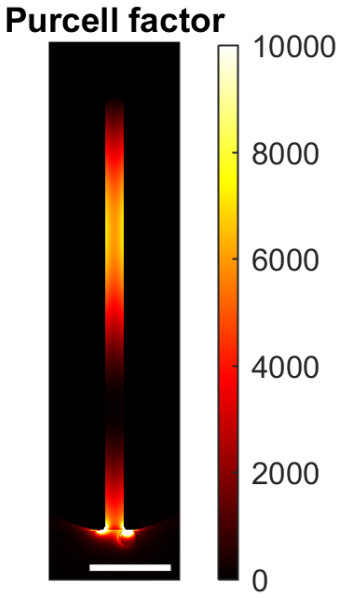

fig. S7. Purcell factor of PNR. The Purcell can reach values of 10000 at the apex and even far beyond inside the PNR. Scale bar: 50nm.

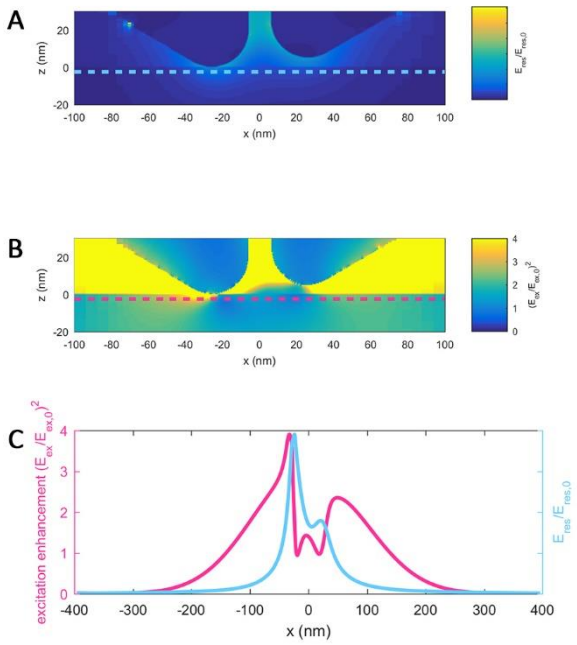

fig. S8. Emission and excitation near-field distribution. (**A**) Near-field distribution of the cavity mode $E_{res}/E_{res,0}$ at 800nm (with temporal apodization). (**B**) Total near-field intensity enhancement distribution $(E_{ex}/E_{ex,0})^2$ after excitation with a Gaussian source at 532nm. (**C**) Cross-section of the field averaged between 2 and 3nm below the PMMA surface (indicated by dashed lines in **A** and **B**). The excitation near-field intensity enhancement $(E_{ex}/E_{ex,0})^2$ (pink) drops before the emission field $E_{res}/E_{res,0}$ (blue) reaches its maximum.

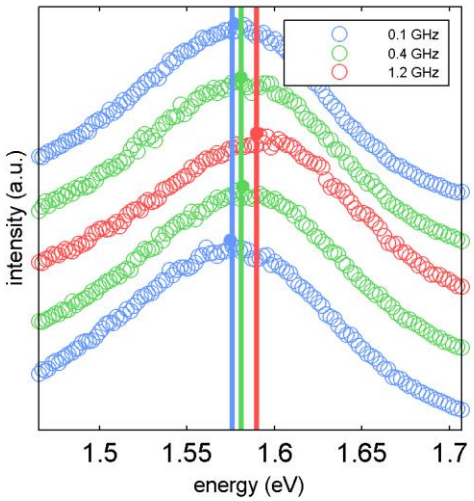

fig. S9. QD resonance shift for high excitation rates. The QD resonance exhibits a reversible blueshift when ramping the excitation rate up and down (bottom to top). Blueshifted BX emission dominates the emission for high excitation rates.

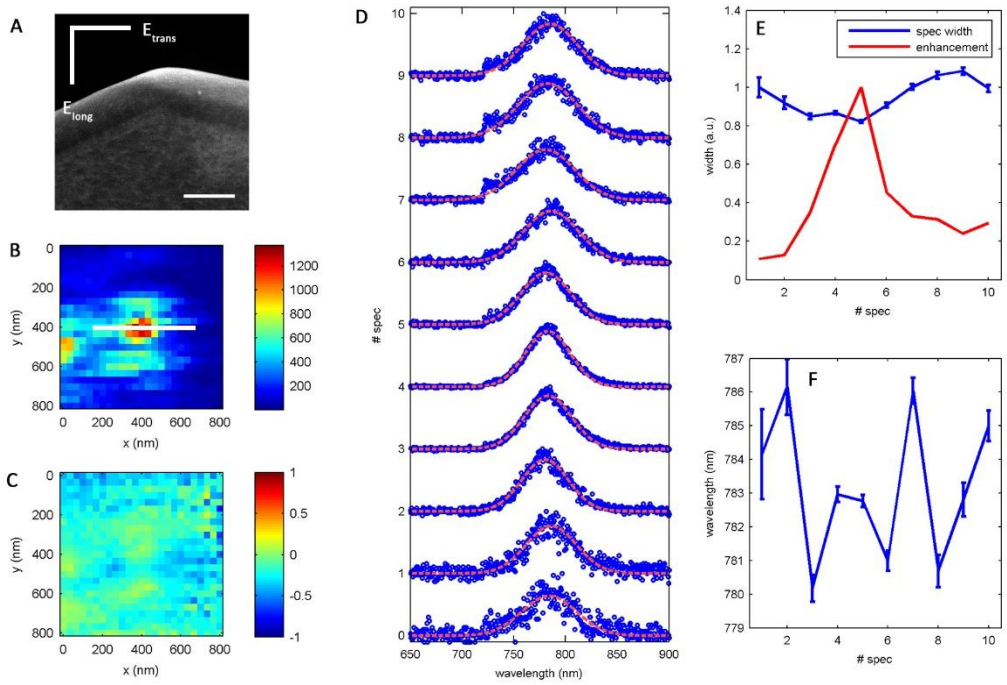

fig. S10. Coupling of a QD to an unstructured gold tip. (**A**) SEM image of an unstructured gold flake. Scale bar: 100nm. (**B**) PL map of the emission of a QD scanned beneath the PNR with the probe centered in the focus. Due to an enhanced excitation field we observe increased fluorescence in close proximity to the unstructured gold tip. (**C**) Degree of polarization (DOP) of the emitted light. No significant change in the DOP can be observed at the location of enhanced fluorescence. (**D**) Spectra (blue circles) measured while moving the QD underneath the tip along the black line as indicated in **B**. When the gold tip moves closer to the QD the amplitude of the spectra increases (all spectra are normalized, the increased amplitude can be deduced from the increased SNR). All spectra are fitted with a Gaussian (red dashed line). (**E**) Width of the Gaussian fit (blue line) and amplitude of the spectra (red line). (**F**) Peak position of the Gaussian fit.

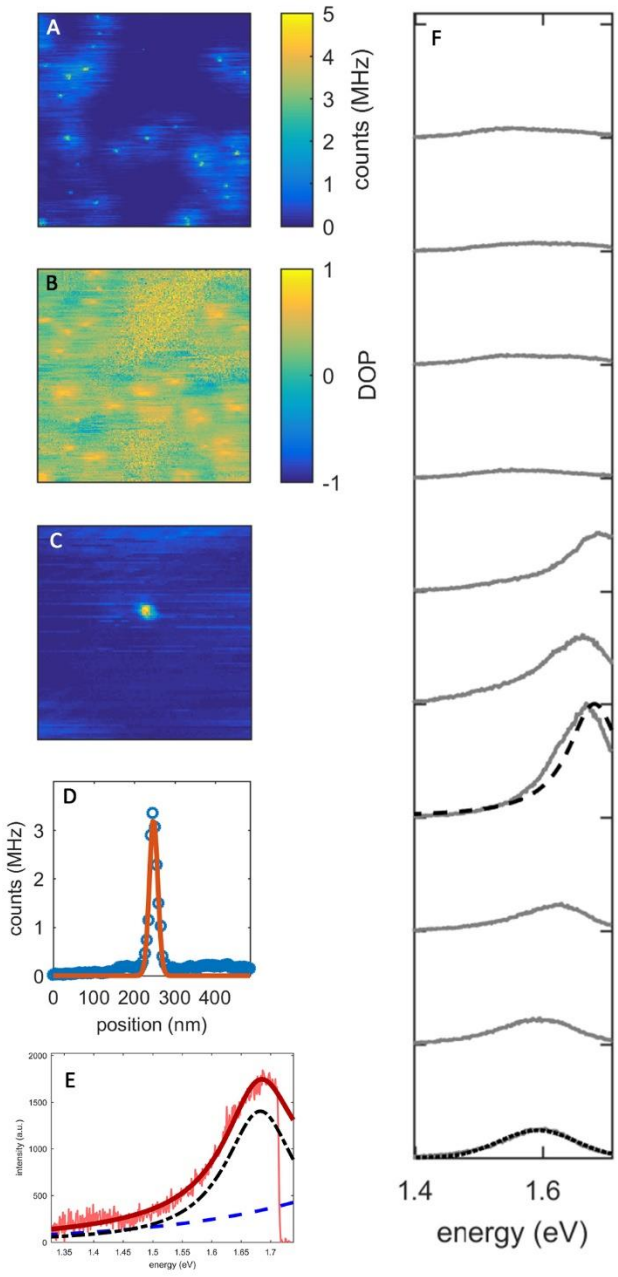

fig. S11. Weak coupling PNR scanning probe. (**A**) PL map of QDs with a weakly coupling PNR centered in the laser focus. (**B**) Degree of polarization of the same region as **A**. The narrow peaks are mostly polarized in transverse direction indicating emission dominantly via the PNR. (**C**) PL map of a single QD. (**D**) Line cut through the QD in **C**. A Gaussian fit shows a FWHM of less than 25nm. (**E**) PL of a PNR and a resonance 735nm. Blue dashed line: Gold photoluminescence background. Black dash dotted line: PNR resonance. Same measurement configuration as in fig. S14. (**F**) Position dependent spectra (gray lines) showing weak coupling. Distance between each spectrum: 20nm. For no coupling (bottom spectrum) the emission from the pure QD can be fitted with a Gaussian (dotted line). At maximum emission (4th from bottom up) the PL spectrum matches the PNR resonance (dashed line).

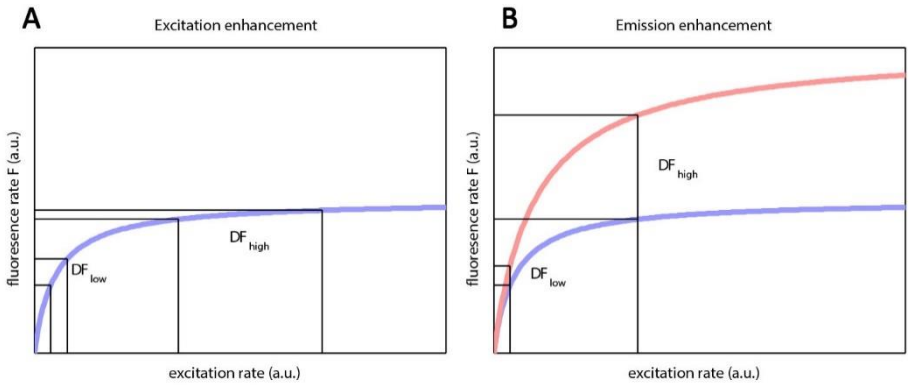

fig. S12. Difference between excitation and emission enhancement. (**A**) Excitation enhancement (factor 2) below saturation (ΔF_{low}) is much more efficient than above the saturation rate (ΔF_{high}). (**B**) Emission enhancement (factor 2, red line) changes the fluorescence characteristic of the emitter. The fluorescence enhancement above saturation is much larger than below saturation.

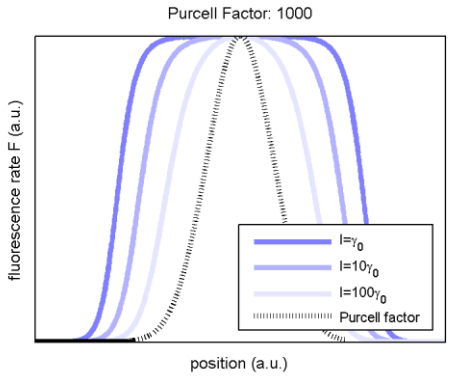

fig. S13. Calculated fluorescence peaks for different excitation rates for an emitter scanned through a Gaussian field profile with a Purcell factor reaching up to 1000. The Purcell factor profile (dashed line) is the theoretical fluorescence profile for an infinitely high excitation rate. Finite excitation rates cause a broadening due to saturation before reaching the maximum Purcell factor.

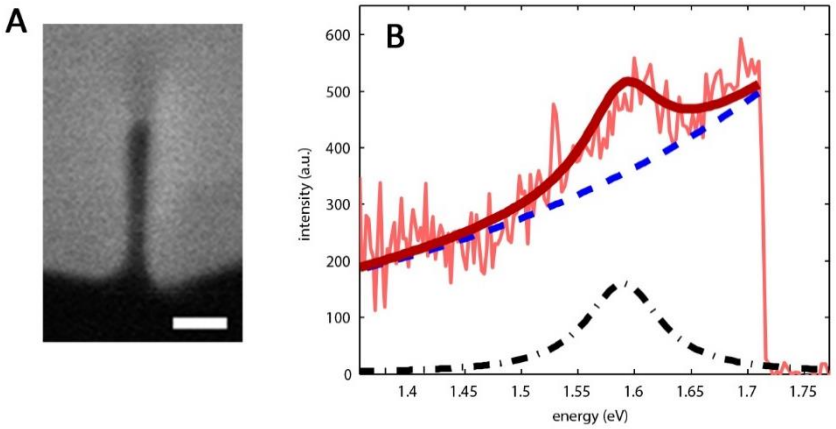

fig. S14. Cavity characterization. (**A**) SEM image of the PNR used for strong coupling recorded at an incident angle of 52° (scale bar 50nm). (**B**) Recorded gold PL emission spectrum of the PNR in A (thin red line). The spectrum is fitted with the sum of an exponential background PL emission (blue dashed line) and the Lorentzian cavity emission (black dash dotted line). The sum of both contributions (thick red line) is in a good agreement with the measured spectrum.

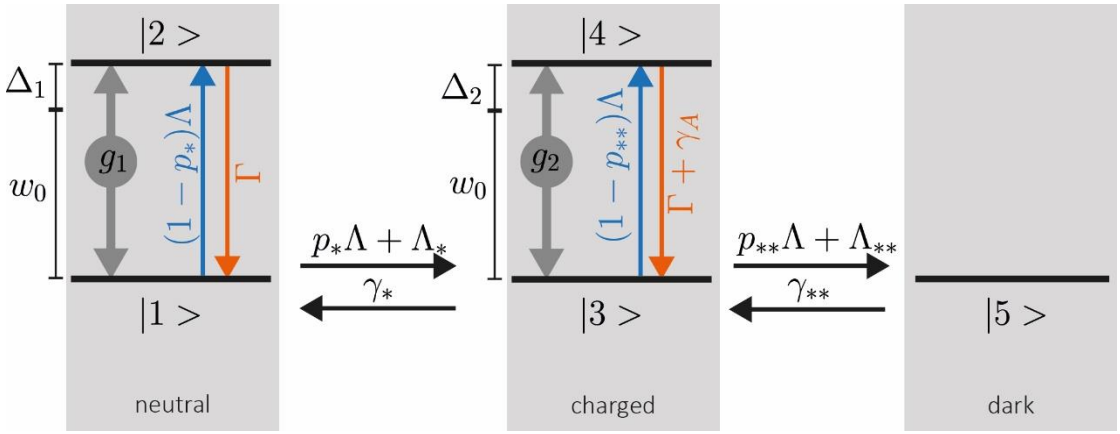

fig. S15. Five-level diagram of the QD. The QD can switch between a neutral, charged (optically active) and dark state, which is optically inactive.

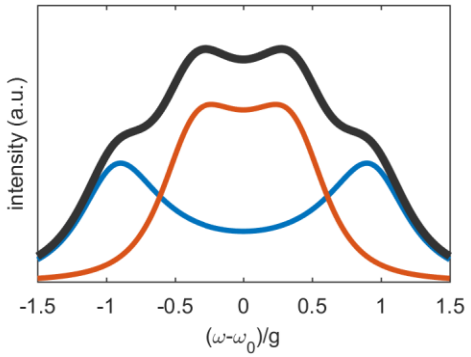

fig. S16. Decomposing the emission of a strongly coupled QD. The neutral (blue) and charged (orange) state have a coupling strength of 1 and 0.5, respectively. Their photon emission rate are equal but the feature of the charged state seems to dominate the spectrum.

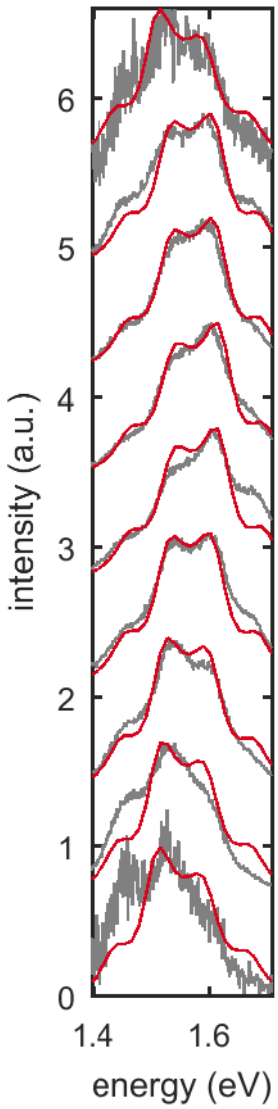

fig. S17. Reversible blue shift for increased excitation rates during SC. The spectra of the strongly coupled QD blueshifts as the excitation rate is increased (spectrum #1-#5, bottom to middle). Gradual reduction of the excitation rate (spectrum #6-#9, middle to top) shows the reverse change of the fluorescence spectra. The measured spectra (gray lines) are overlayed with the spectra obtained from the quantum-model (red lines) where we adjusted the QD detuning for the neutral and the charged state.

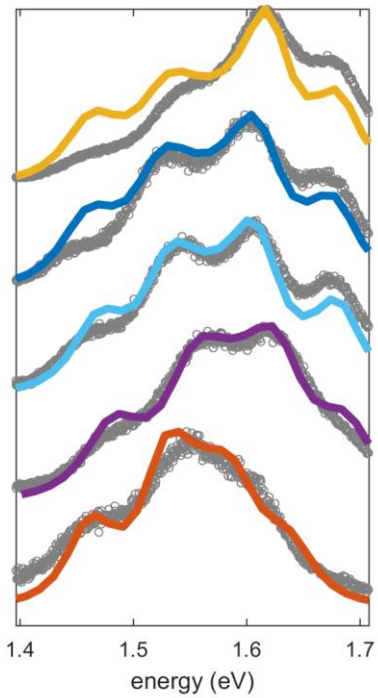

fig. S18. Collection of spectra of five different QDs in SC with the PNR. The measured spectra (open circles) are ordered by the detuning of the excitonic resonances. Each spectrum was fitted individually with the quantum optical model (solid lines). The coupling strength, detuning as well as the QD resonance can vary due to structural variations of the QDs (size, orientation).

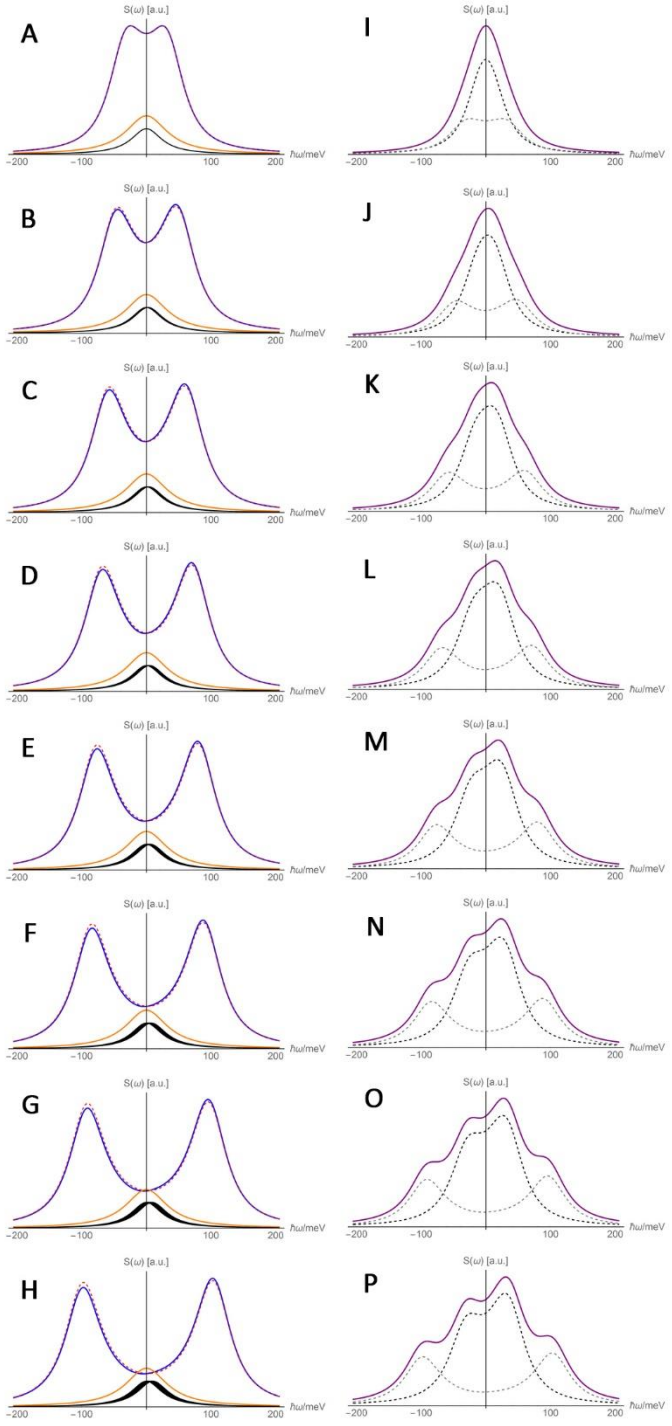

fig. S19. Collective coupling of a multilevel emitter with a resonant cavity. (**A**-**H**) The plasmon resonance (orange line) couples with one (a) to eight (h) levels (black lines). The corresponding coupled spectrum (blue line) calculated with H_{mic} indicates the transition into two symmetric Rabi peaks. The coupled spectrum calculated via H_{eff} (red dashed line) yields similar results. (**I**-**P**), Superposition of two multi-level systems with coupling

strength g_1 and g_2. Increasing the number of levels from one (I) to eight (P) shows the transition into a four peaked spectrum.

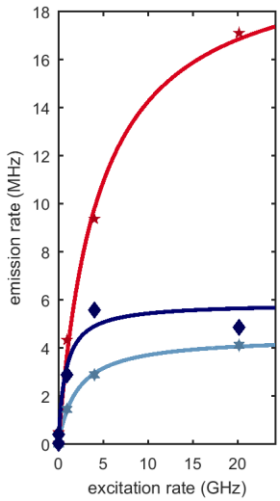

fig. S20. Saturation of the strongly coupled system. Measured fluorescence saturation (markers) for different QDs in strong coupling conditions fitted according to the saturation behavior predicted by the quantum optical model (solid lines).